Supplementary Materials

Materials and Methods

Figures S1-S13

Tables S1-S7

Movies S1-S3

References (22–47)

Materials and Methods

Aβ(1-42) sample and fibril preparation

Recombinantly produced [*U*-^{13}C,^{15}N]-Aβ(1-42) (95% purity) (with Asp1 as N-terminal amino acid residue) was purchased from Isoloid GmbH (Düsseldorf, Germany). Reverse phase high performance liquid chromatography (RP-HPLC) was applied leading to 98.5% purity. RP-HPLC was performed on a semipreparative Zorbax SB-300 C8 column (9.4 mm diameter, 250 mm length, Agilent, Böblingen, Germany) connected to an Agilent 1260 Infinity system with UV detection at 214 nm and a column temperature 80°C. The mobile phase used was 30% v/v acetonitrile (ACN), 0.1% (v/v) trifluoroacetic acid (TFA) in water. Under these conditions [*U*-^{13}C,^{15}N]-Aβ(1-42) elutes as monomers (*22*). Conversion of monomeric [*U*-^{13}C,^{15}N]-Aβ(1-42) to several µm long, unbranched fibrils occurred over several weeks by undisturbed incubation of the collected [*U*-^{13}C,^{15}N]-Aβ(1-42) fraction directly in the mobile phase as solvent at room temperature. After 8 weeks no monomeric [*U*-^{13}C,^{15}N]-Aβ(1-42) was detectable by analytical RP-HPLC in supernatants of centrifuged (16,100 x *g*) fibrils.

To ensure complete comparability of the data, all experiments, notably cryo-EM, solid-state NMR, AFM, and X-ray diffraction, were done on [*U*-^{13}C,^{15}N]-Aβ(1-42) fibrils prepared under identical conditions described above.

Cell viability assay

3-(4,5-Dimethylthiazol-2-yl)-2,5-diphenyltetrazolium bromide (MTT) based cell viability assays were performed to investigate the cytotoxicity of [*U*-^{13}C,^{15}N]-Aβ(1-42) fibrils either grown over weeks in aqueous 30% ACN/0.1% TFA, pH 2 under quiescent conditions at RT or grown over night in 50 mM Na-phosphate, pH 7.4 at 37°C and 300 rpm shaking. Fibrils were sedimented by centrifugation (20 min, 3,000 x *g*), resuspended in 250 µl of the respective fibril growth solvens and ultrasonicated (Bandelin Sonopuls, sonotrode MS72, Bandelin, Berlin) with following settings: 5-times ultrasonication for 1 sec, 4 sec pause, 10% power, ice cooling. Fibril concentrations expressed as Aβ(1-42) monomer equivalents of 120.5 µM (grown in aqueous ACN/TFA, pH 2) or 62.5 µM (grown in Na-phosphate, pH 7.4) were determined by analytical RP-HPLC (*22*).

Rat pheochromocytoma PC12 cells (Leibniz Institute DSMZ, Braunschweig, Germany) were cultivated in DMEM medium supplemented with 10% fetal bovine serum and 5% horse serum. 10,000 cells per well were seeded on collagen-coated 96 well plates (Gibco, Life technology, Carlsberg, USA) and incubated in a 95% humidified atmosphere with 5% CO_2 at 37°C for 24 h.

Fibrils were added at final concentrations of 3, 1, 0.3, 0.1 or 0 µM (expressed as Aβ(1-42) monomer equivalents) to PC12 cells. After further incubation for 24 h in 95% humidified atmosphere with 5% CO_2 at 37°C cell viability was measured using the Cell proliferation Kit I (MTT) (Roche, Basel, Switzerland) according to the manufacturer's instruction. The absorbance of the formazan product was determined by measuring at 570 nm after subtracting the absorption at 660 nm in a Polarstar Optima plate reader (BMG, Offenburg, Germany). All results were normalized to cells that were treated with the

respective fibril growth solvent only (final concentrations are 0.75% ACN/0.0025% TFA or 2.4 mM Na-phosphate, respectively).

Atomic force microscopy

For initial inspection of the sample atomic force microscopy (AFM) was used and results were consistent with negative stain EM images (figs. S1 and S2). AFM imaging was performed under air dried conditions in intermittent contact mode at a line rate of 0.5 to 1 Hz in a JPK Nano Wizard 3 atomic force microscope (JPK instruments, Berlin, Germany) using a silicon cantilever with silicon tip (OMCL-AC160TS, Olympus, Germany) with a typical tip radius of 7 ± 2 nm, a force constant of 26 N/m. Images were processed using the JPK Data Processing software. Aβ(1-42) fibrils grown in aqueous 30% ACN/0,1% TFA were directly applied (10 µl) on freshly cleaved Mica and dried on air before measurement.

Grid preparation and image acquisition for cryo-EM

For more detailed sample inspection, negative stained fibrils were prepared on 400 mesh carbon-coated copper grids (S160-4, Plano GmbH, Germany), stained with 1% uranyl acetate, and imaged using a Libra120 electron microscope (Zeiss) operated at 120 kV (figs. S1A and B). For the cryo-preparation, glow-discharged holey gold films (UltrAuFoil R 1.2/1.3 300 mesh, Quantifoil) were used. A sample volume of 2.5 µl was applied to the grid, blotted for 2.5 s, and then cryo-plunged using a Vitrobot (FEI).

In total 2026 micrographs at a magnification of 110,000 were collected on a Tecnai Arctica (200 kV) with a field emission gun using a Falcon III (FEI) direct electron detector directed by the data collection software EPU (fig. S1C). Each micrograph was composed of 80 frames, aligned by proprietary software of the microscope manufacturer. The samples were exposed for 2 s to an integrated flux of 24 $e^-/Å^2$ at an underfocus ranging between 0.5 and 1.5 µm. The pixel size was 0.935 Å, as calibrated using gold diffraction rings within the powerspectra of a cross grating grid (EMS, Hatfield).

Cryo-EM Image processing

All image processing tasks were performed with the EMAN2/SPARX software package (*23, 24*). The micrographs were examined with the SPARX program *cter* (*25*) to determine defocus and astigmatism parameters. Only those micrographs were chosen for further processing, which contain significant signal beyond a resolution of 6 Å as provided in the *cter* output (column 15:"frequency at which the signal drops by 50% due to estimated error of defocus alone"). This criterion resulted in 995 micrographs from which in total 3179 fibrils were picked manually using *helixboxer*. Individual fibril segments were extracted from the fibril images with a 90% overlap, which yielded 127,765 segments. The length of the segments is 216 pixel (or 201.96 Å) with a pixel size 0.935 Å.

A strong peak at 4.67 Å was clearly visible in the summed powerspectrum of all fibril segments. The cross-β pattern with the ~4.7 Å spacing can even be seen in some of the raw micrographs of individual fibrils (see fig. S1E). Also in the helical symmetry search, which was at first performed with C_2 symmetry, the optimal rise parameter was 4.67 Å. This is in close agreement with fiber diffraction data, which finds the corresponding strong peak at 4.65 Å (cf. Fig. 3C and fig. S9). A later search for helical

symmetry parameters without C_2 symmetry yielded an optimum for a helical rise of (2.335±0.04) Å and an azimuthal rotation of (-179.275±0.025)°. The error on the axial rise is estimated from the estimated pixel size of 1.5 % and the error on the azimuthal rotation is given by the step-size of the sampling during the symmetry parameter search. The resulting helical pitch is (1160±199) Å. This choice of the symmetry parameters lead to a clear separation of β-strand density along the fibril. The helical symmetry corresponds to an approximate 2_1 screw symmetry with a rise of 4.67 Å. This helical symmetry leads to a staggered arrangement of subunits, which is clearly visible already in the 2D class averages (fig. S10). An initial reconstruction with all images was calculated with the *sxhelicon.py* program using a noisy cylinder as a starting model. This initial reconstruction was then filtered to 20 Å and used as an initial model for the next round of refinement (using the program *sxheliconlocal.py*). Cross-correlation coefficients (CC) were computed for each particle image by projection matching with the current initial model. Since the CC is directly correlated with defocus (correlation coefficient of 0.855), these CC values averaged over all segments from each fibril were then plotted against the defocus values (fig. S13B). Those 813 fibrils with an average CC value above the line defined by y=0.855*x+0.3 were selected for the final round of refinement to reach higher resolution with a consistent set of images. These 813 fibrils correspond to ~25% of all picked fibrils and contain 27,132 segments. Applying the helical symmetry leads to in total ~295,000 asymmetric units.

The resolution of the final reconstruction was estimated to 4.0 Å by the even/odd FSC 0.143 criterion (see fig. S13C). For the calculation of the FSC, the data set was split after the final refinement by whole fibrils, i.e. none of the segments in the even set overlap with segments in the odd set and vice versa. The comparison between the full density reconstruction and a density map computed from the model by FSC yields a cross-resolution of 4.5 Å (with the 0.5-criterion). Comparison of nine subunits of the atomic model with a density map masked around this model yields a cross-resolution of 4.1 Å. The final density map was processed by the EMAN2 processor *filter.lowpass.autob* (B-factor of -501 $Å^2$), further sharpened by applying a B-factor of -50 $Å^2$, and filtered to 4.0 Å.

Model Building and Refinement

The atomic model was built in Coot (*26*). A fragment of the fibril consisting of 9 subunits was refined with PHENIX (*27-29*) in real space (*phenix.real_space_refine*) using a resolution cut-off of 4.0 Å. NCS restraints between all 9 chains were applied. At a later stage of model refinement select backbone hydrogen bonds between chain *i* and *i*+2 were restrained. Grouped B-factor refinement was performed, which yields an average atomic B-factor of 88.6 $Å^2$. Table S1 shows details of the refinement.

In total three hydrophobic sidechains per subunit are exposed to the solvent (Val12, Val18, and Phe20, cf. Fig. 2). On the surface, the sidechain of Phe20 seems to exist in two rotamers with about equal occupancy. This is supported by the EM density and in perfect agreement with the observed resonance doubling for Phe20 and Ala21 in the NMR spectrum (cf. figs. S8 E and F). In addition, also Ser26 exhibits a second set of resonances, which is in agreement with the fact that the density map around Ser26 suggests the presence of a second conformer with smaller occupancy (fig. S8B). This

second conformer would cross the trace between Ser26 and Lys28 from layer *i* into the layer *i*+2, however, it was not possible to further classify the images to clearly resolve this second conformer. An obvious extra density between the positively charged sidechains of His14 and Lys16 is likely the only anion available under the fibrillation conditions, a trifluoroacetate ion (fig. S8C).

Solid-state NMR experiments, site-specific resonance assignment, distance constraints and data analysis

Magic-angle spinning (MAS) NMR spectra were recorded at Varian INOVA spectrometers at fields of 14.1 Tesla and 18.8 Tesla (corresponding to ^{1}H resonance frequencies of 600 and 800 MHz, respectively), equipped with 3.2 mm standard bore triple-resonance MAS probe heads. All experiments were performed on one single uniformly labeled [*U*-^{13}C,^{15}N]-Aβ(1-42) sample which was obtained from the same preparation as the fibrils used for EM, AFM, and X-ray diffraction. The sample pellet containing ~10 mg of protein was directly centrifuged into a 3.2 mm Varian rotor. The rigidity of the sample was probed by complementing cross-polarization based excitation schemes, which by dipolar transfer selectively excite rigid regions of the sample with an INEPT experiment where the through-bond magnetization transfer from ^{1}H to ^{13}C leads to selective excitation of mobile regions (*30*). Whereas the INEPT spectrum recorded at a sample temperature of 20 ± 5 °C did not show any observable signals (data not shown), in cross-polarization based spectra recorded at a sample temperature of 0 ± 5 °C resonances for all 42 amino acid residues were visible. Line-widths in 2D spectra were 0.5 ppm in the carbon and 1.1 ppm in the ^{15}N dimension. For sequential resonance assignment several types of multi-dimensional homo- and heteronuclear correlation spectra were recorded (table S2).

To gather information about the ^{13}C backbone and side chain resonances, we performed proton-driven spin diffusion (PDSD) experiments with different mixing times from 20 ms to 750 ms. At a mixing time of 200 ms, also sequential interresidual correlations between side chain and backbone atoms could be obtained (fig. S6A). To identify and confirm one-bond correlations, we recorded an additional homonuclear double quantum correlation experiment with SPC5-recoupling (*31*).

Inter-residual correlations could be confirmed in ^{15}N/^{13}C correlation spectra. Frequency selective polarization transfer from amide ^{15}N to ^{13}C CA or CO is achieved by specific CP(*32*). Subsequently, polarization is transferred to the side-chain carbon atoms via DARR mixing (*33*) or by a band selective homonuclear CP (BSH CP)(*34*) with subsequent DREAM mixing (*35*). Several NCACX and NCOCX-type spectra were used for a backbone walk (figs. S6 B and C). ^{15}N sidechain resonances of lysine, histidine and arginine residues could be identified from a 1D ^{15}N CP spectrum. Long-range correlations could be obtained from a PDSD spectrum recorded with a mixing time of 750 ms as well as from a CC correlation spectrum obtained with Proton Assisted Recoupling (PAR) (*36*) (fig. S7).

During all acquisition and evolution times high-power broadband proton decoupling with SPINAL phase modulation with an rf intensity of about 83 kHz was applied (*37*). All spectra were processed with nmrPIPE (*38*) using squared and shifted sine-bell apodization. ^{13}C chemical shifts were externally referenced using an adamantane sample. The CH signal of adamantane was set to 31.4 ppm (corresponding to the DSS reference

scale. ^{15}N chemical shifts were indirectly referenced to liquid NH_3 based on ^{13}C shifts and assigned in CCPN (*39*). Secondary chemical shifts (Fig. 3B) were referenced to acidic random coil shifts at pH 2.3 and 8 M urea(*40*).

We could assign all amino acids in the protein sequence (table S3, Fig. 3A, figs. S5-S7, BMRB accession code 27212). Except for three residues (Phe20, Ala21 and Ser26), all amino acids only give rise to one single set of resonances, underlining the structural homogeneity of the fibrils. Histidine $^{15}N\delta1$ and $^{15}N\delta2$ side-chain chemical shifts of 182.6 ppm and 176.1 ppm, respectively, are characteristic of biprotonated imidazole rings, as expected at a pH value of 2 (*41*). Despite the low pH, the relatively high Cγ NMR resonance shifts of the amino acid residues Asp1 and Asp7 suggest that the side chains of these residues are to a high degree deprotonated, which is consistent with salt bridge formation of Asp1 with Lys28, and Asp7 with Arg5 (*42*). Likewise, the Cδ resonance shift of Glu11 indicates a predominantly deprotonated state, which supports the finding that this residue forms salt bridges with the positively charged side-chains of His6 and His13.

NMR cross-peaks in PDSD spectra with long mixing times (fig. S6 and fig. S7A) and the PAR (*36*) spectrum (fig. S7B) which are not due to sequential contacts are in agreement with the cryo-EM structure, corresponding to middle and long-range contacts Gly33-Met35, Met35-Gly37, Ile32-Met35, Val12-His14, Gly29-Ala42, Ala2-Val36, Ile32-Val40 and Ala42-Lys28.

X-ray diffraction experiments

Droplets of Aβ(1–42) centrifuged fibrils in fibrillation solution were placed between glass capillary supports and allowed to dry (*43*) and subsequently mounted on a standard pin-holder. Wide-angle data sets were collected at the beamline P11 at DESY, Hamburg, at a wavelength of 1.0332 Å with a pin-hole generated beam size of 50 µm. The data showed the strong rings typical for un-oriented amyloid samples at 9.72 Å, 4.65 Å, and 3.7 Å (Fig. 3C). They were processed and analyzed with FIT2D (*44*). The observed rings were integrated to obtain 1D-spectra (fig. S9), which were used for comparison with calculated diffraction for a cell containing the single Aβ(1–42) fibril model from electron microscopy (CCP4) (*45*). The superposition showed a reasonable agreement between the model and the observed X-ray diffraction for the characteristic scattering of un-oriented fibrils. The previously described doublet of the 4.7 Å peak is not resolved here (*46*).

Supplementary Text

Author contributions

L.G. designed research and prepared fibrils. J.L. and L.G. performed X-ray diffraction experiments. D.S. and H.H. performed NMR experiments and data analysis. R.R. and G.F.S performed electron microscopy experiments. E.R. and L.G. performed AFM experiments. M.T. and L.G. performed cell viability experiments. C.S. and G.F.S. performed EM data processing. All authors discussed the results. L.G., W.H., H.H., D.W., and G.F.S wrote the paper with input from all authors.

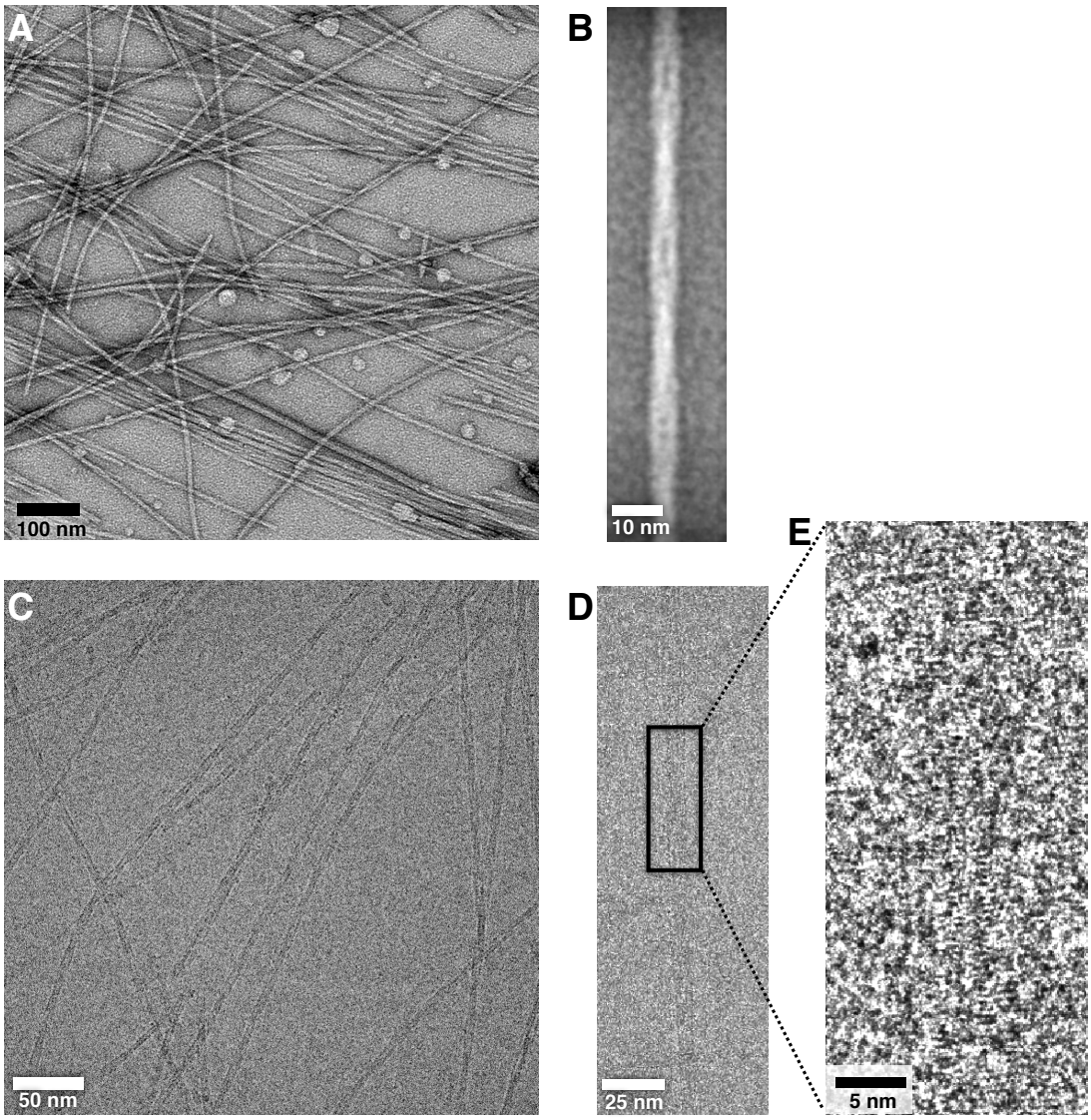

Fig. S1.

Representative micrographs. (**A**) Micrograph of negative stained fibrils and (**B**) average over three aligned fibril segments. (**C**) Cryo-EM micrograph (defocus of 1.28 μm). (**D**) and (**E**) The typical density pattern from β-strands separated by ~4.7 Å is visible directly in some of the micrographs at small defocus.

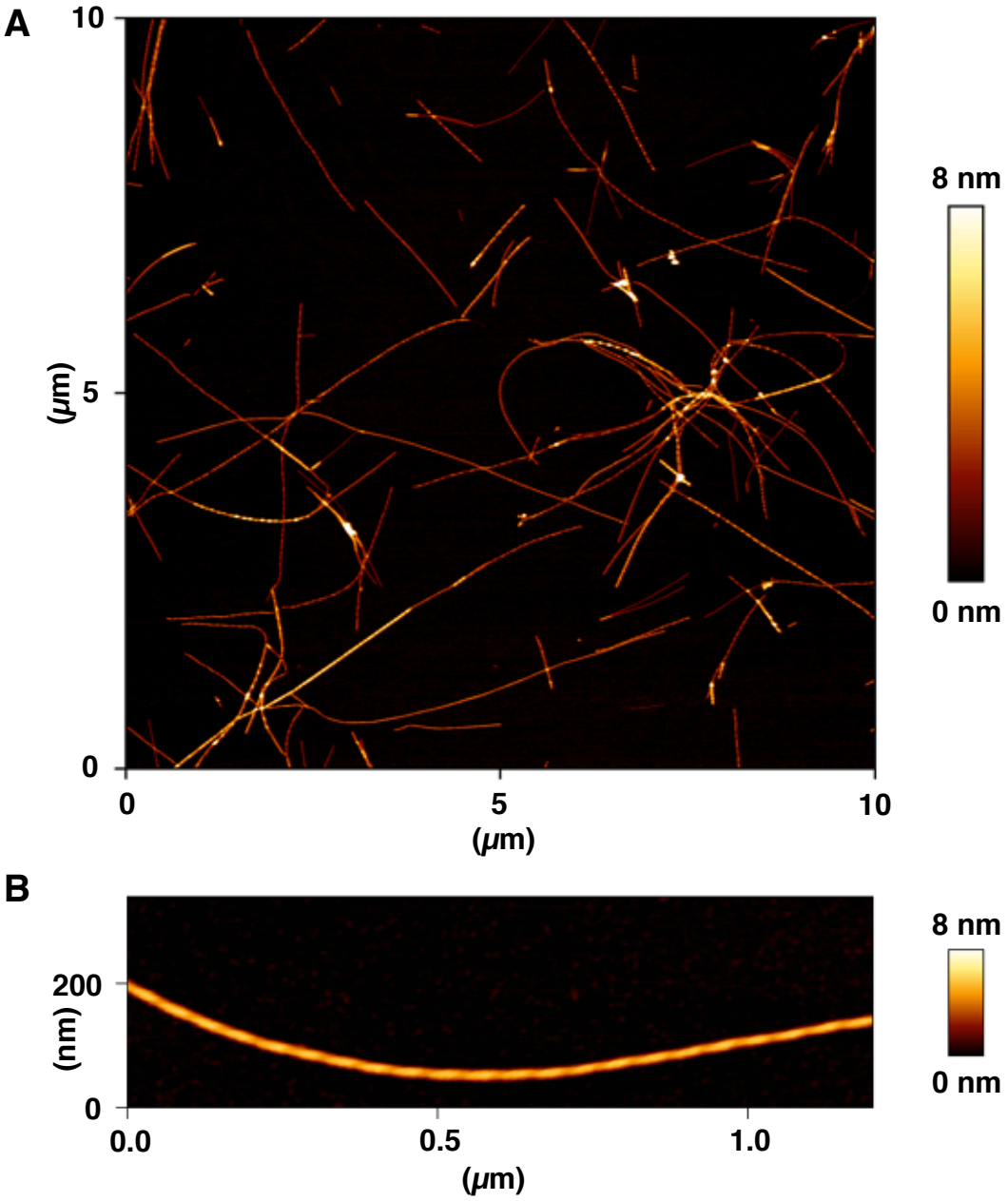

Fig. S2

Atomic force microscopy of Aβ(1–42) fibrils. (**A**), (**B**) Fibrils grown in 30% ACN, 0.1% TFA, pH 2. Shown is an overview (**A**) and a representative fibril (**B**).

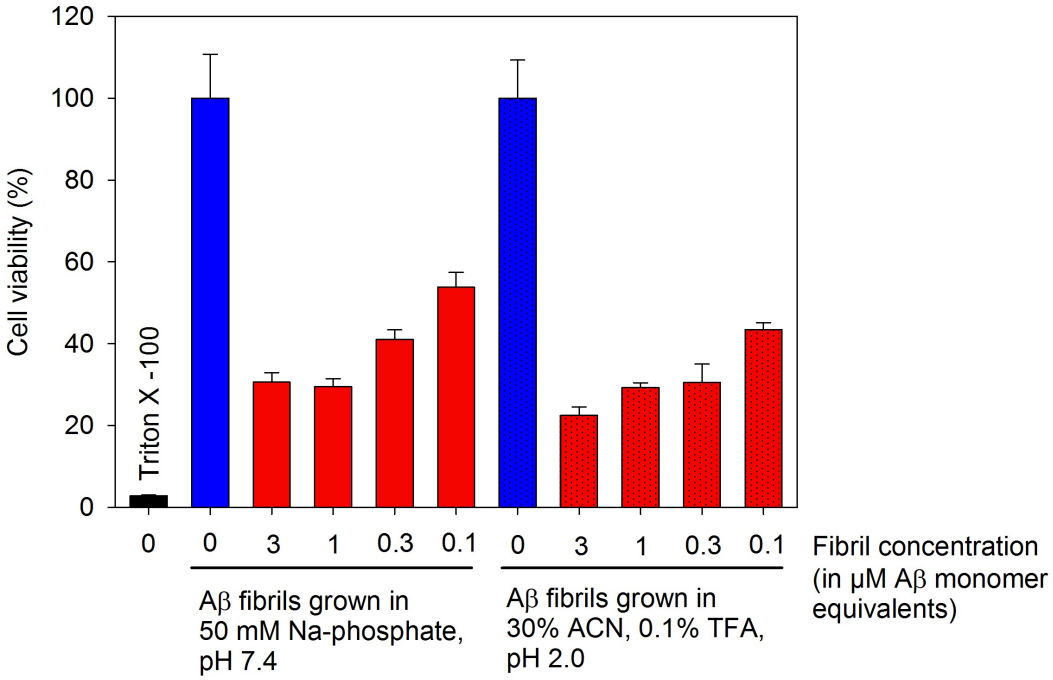

Fig. S3

Cell toxicity. Cell toxicity of Aβ(1-42) fibrils prepared under different fibrillization conditions on PC12 cells. Aβ fibrils prepared using indicated solvent conditions were tested at the given concentrations for toxicity on PC12 cells (red bars). Cells treated with 0.125% Triton X-100 were used as a positive control (black bar). Results were normalized to cells treated with the respective fibril growth solution only (blue bars). Values are means +/- SD of 5 replicates.

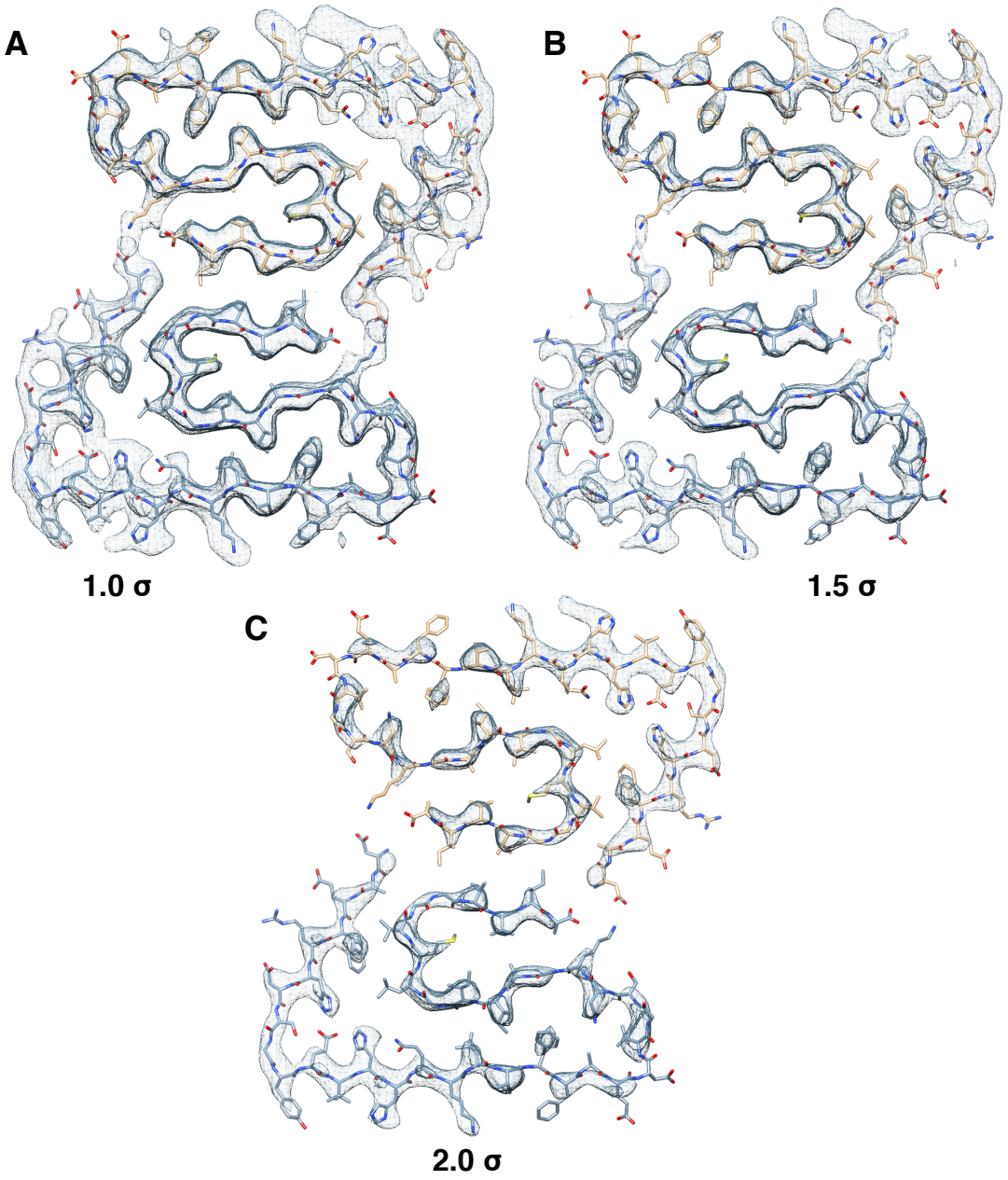

Fig. S4

Density map at different thresholds. Showing the cross-section of the density map as in Fig. 2 with different density thresholds, (**A**) at 1 σ, (**B**) 1.5 σ, and (**C**) at 2 σ.

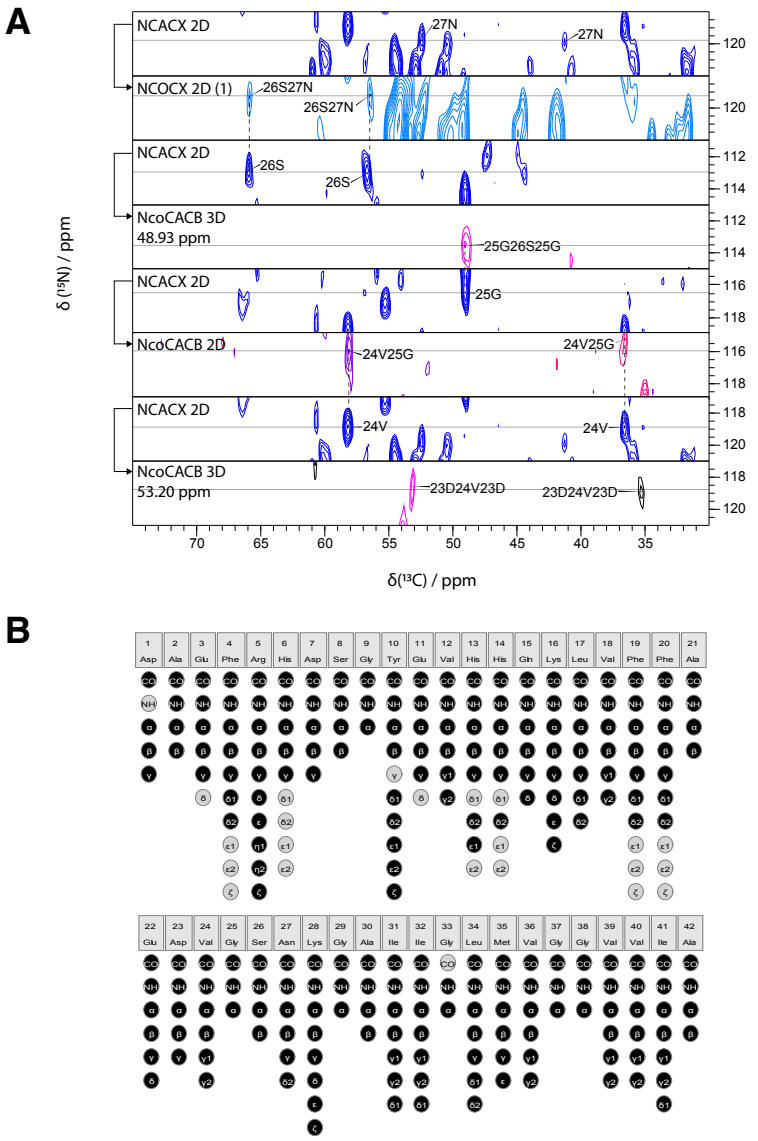

Fig. S5

NMR resonance assignment. (**A**) Representative strip plot of 2D NcoCX (light blue), 2D NcaCX (dark blue) and 2D/3D NcoCACB (purple/pink) spectra illustrating the resonance assignment of amino acids Asp23 to Asn27. All spectra, except for the NCOCX 2D (*32*), were recorded at a magnetic field strength of 18.8 T corresponding to a proton Larmor frequency of 800 MHz, a sample temperature of T = 0 ± 5 °C and a spinning speed of 18 kHz. The NCOCX 2D (*32*) was recorded at a magnetic field strength of 14.1 T corresponding to a proton Larmor frequency of 600 MHz, a sample temperature of T = 0 ± 5 °C and a spinning speed of 14 kHz. A squared and shifted sine bell function was used for apodization (shift between 0.28·π and 0.33·π). (**B**) All assigned carbon and nitrogen atoms of the fibrillar Aβ(1–42) are shown by black circles, unassigned atoms are shown in grey. The assignment graph was exported from the software CcpNMR 2.3.

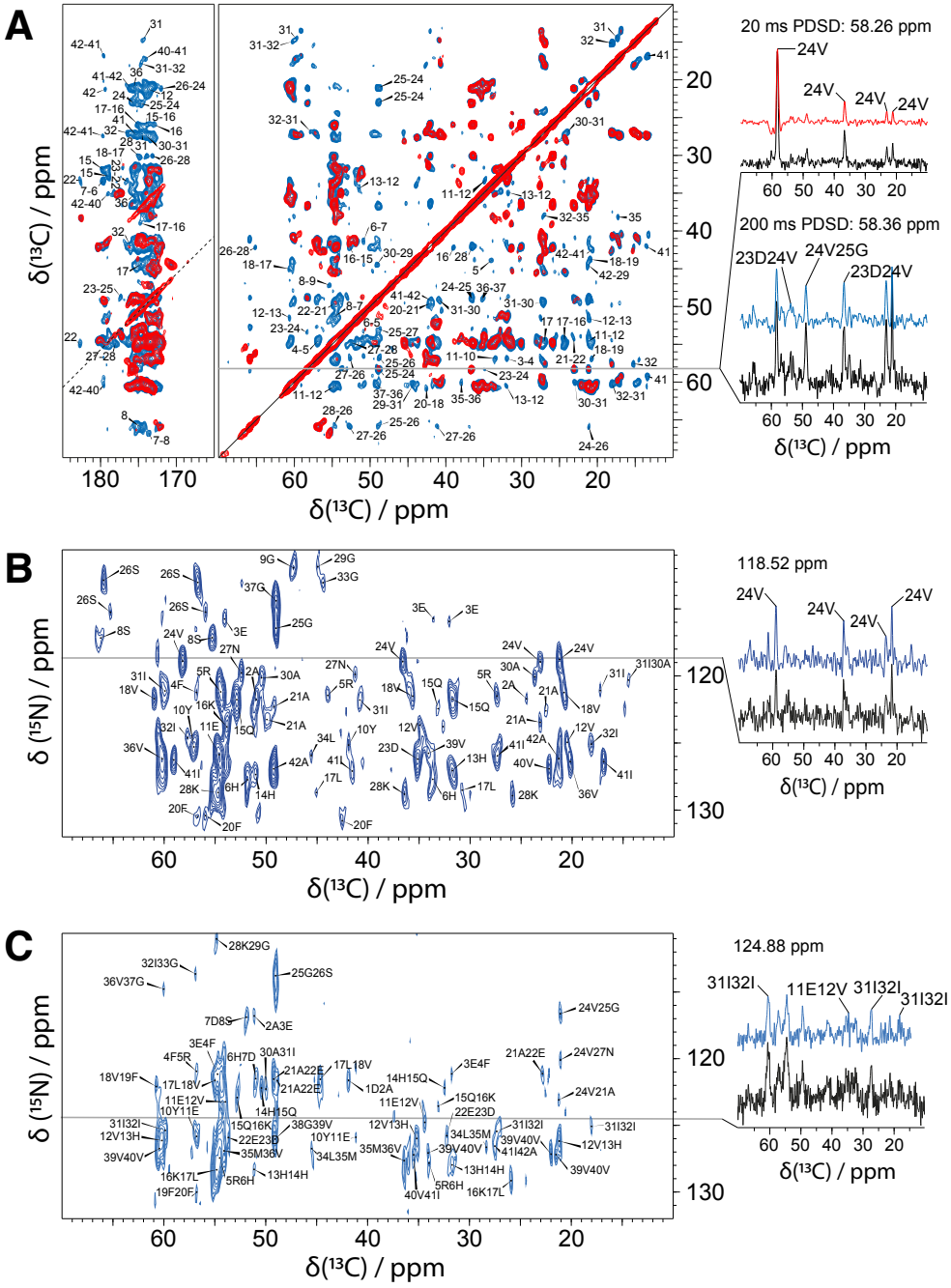

Fig. S6

Proton-Driven Spin Diffusion (PDSD) and ^{15}N/^{13}C correlation NMR spectra of fibrillar Aβ(1–42). All spectra were recorded at a magnetic field strength of 18.8 T corresponding to a proton Larmor frequency of 800 MHz and a sample temperature of T = 0 ± 5ºC. (**A**) Overlay of two PDSD spectra, which were recorded at a spinning speed of 12.5 kHz. For homonuclear ^{13}C/^{13}C mixing, PDSD with a mixing time of 20 ms (red

contours) and 200 ms (blue contours) was employed. The spinning speed was chosen close to the rotational resonance (R2) condition and facilitates magnetization transfer between Cα and CO of neighboring amino acid residues. Sequential information is provided via cross-peaks of amino acids in close spatial proximity. A squared and shifted sine bell function was used for apodization (shift of $0.30 \cdot \pi$ for the 20 ms spectrum and $0.28 \cdot \pi$ for the 200 ms spectrum). Contour levels increase by successive factors of 1.2. Representative 1D slices taken from the processed (red and blue traces, respectively) and from the corresponding unprocessed (black traces) 2D spectra are displayed at 58.26 ppm for the 20 ms spectrum and at 58.36 ppm for the 200 ms spectrum. (**B**) and (**C**) $^{15}N/^{13}C$ correlation NMR spectra recorded at a spinning speed of 18 kHz. (**B**) 2D NCACX correlation spectrum. For homonuclear $^{13}C/^{13}C$ mixing, DARR with a mixing time of 55 ms was employed. (**C**) 2D NCOCX correlation spectrum. For homonuclear $^{13}C/^{13}C$ mixing, DARR with a mixing time of 107.5 ms was employed. Carbon sidechain and backbone shifts of amino acid (*i*) are correlated with the nitrogen backbone shift of the following amino acid in the sequence (*i*+1). A squared and shifted sine bell function was used for apodization for both spectra (shift of $0.28 \cdot \pi$). Contour levels increase by successive factors of 1.2. 1D slices taken from the processed (blue trace) and unprocessed (black trace) 2D NCαCX spectrum are given at a ^{15}N chemical shift of 118.52 ppm; 1D slices taken from the processed (blue trace) and unprocessed (black trace) 2D NCOCX spectrum are given at a ^{15}N chemical shift of 124.88 ppm.

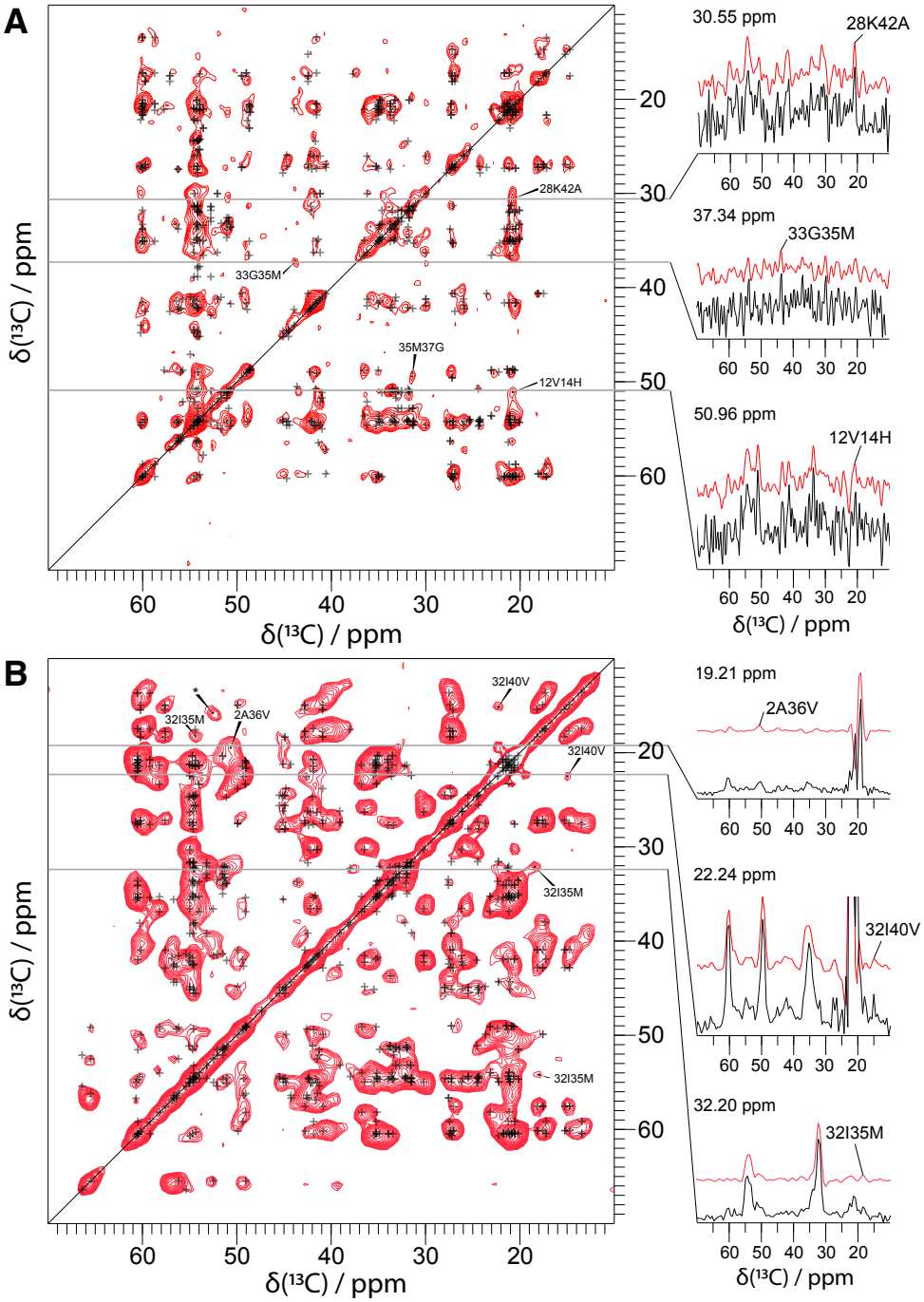

Fig. S7

750 ms PDSD and 15 ms PAR spectra. (**A**) Proton-driven spin diffusion (PDSD) spectrum showing $^{13}C/^{13}C$ correlations of fibrillar Aβ(1–42). The spectrum was recorded at a magnetic field strength of 14.1 T corresponding to a Larmor frequency of 600 MHz, a sample temperature of T = 0 ± 5ºC and a spinning speed of 15 kHz. For homonuclear $^{13}C/^{13}C$ mixing, PDSD with a mixing time of 750 ms was employed. Sequential and

structural information is provided via cross-peaks of amino acids in close spatial proximity, and additional contacts not shown in fig. S6 are assigned in the spectrum. Black crosses indicate intraresidual and sequential cross-peaks, predicted up to 7 bonds between neighboring amino acids (only labels for cross-peaks which can be observed in the spectrum are displayed). A squared and shifted sine bell function was used for apodization (shift of $0.40 \cdot \pi$). Contour levels increase by successive factors of 1.2. 1D slices taken from processed (red trace) and unprocessed (black trace) 2D spectra are displayed at 30.55 ppm, 37.34 ppm and 50.96 ppm, respectively. (**B**) Overlay of a Proton-Assisted Recoupling (PAR) spectrum (red) and a PDSD spectrum (black) showing $^{13}C/^{13}C$ correlation of fibrillar Aß(1–42). The PAR spectrum (*36*) was recorded at a magnetic field strength of 14.1 T corresponding to a proton Larmor frequency of 600 MHz, a sample temperature of T = 10 ± 5 °C and a spinning speed of 20 kHz. For homonuclear $^{13}C/^{13}C$ mixing, PAR with a mixing time of 15 ms was employed. The PDSD spectrum (for assignments see Fig. 3A and fig. S6A) was recorded at a magnetic field strength of 18.8 T corresponding to a proton Larmor frequency of 800 MHz, a sample temperature of T = 0 ± 5°C, a spinning speed of 12.5 kHz and a mixing time of 20 ms. Sequential and structural information is provided via cross-peaks of amino acids in close spatial proximity in both spectra. Assignments for additional contacts not shown in fig. S6 are indicated in the PAR spectrum. Black crosses indicate intraresidual and sequential cross-peaks, predicted up to 7 bonds between neighboring amino acids (only labels for cross-peaks which can be observed in the spectrum are displayed). A squared and shifted sine bell function was used for apodization (shift of $0.30 \cdot \pi$). Contour levels increase by successive factors of 1.2. 1D slices taken from processed (red trace) and unprocessed (black trace) 2D spectra are displayed at 19.21 ppm, 22.24 ppm and 32.30 ppm, respectively.

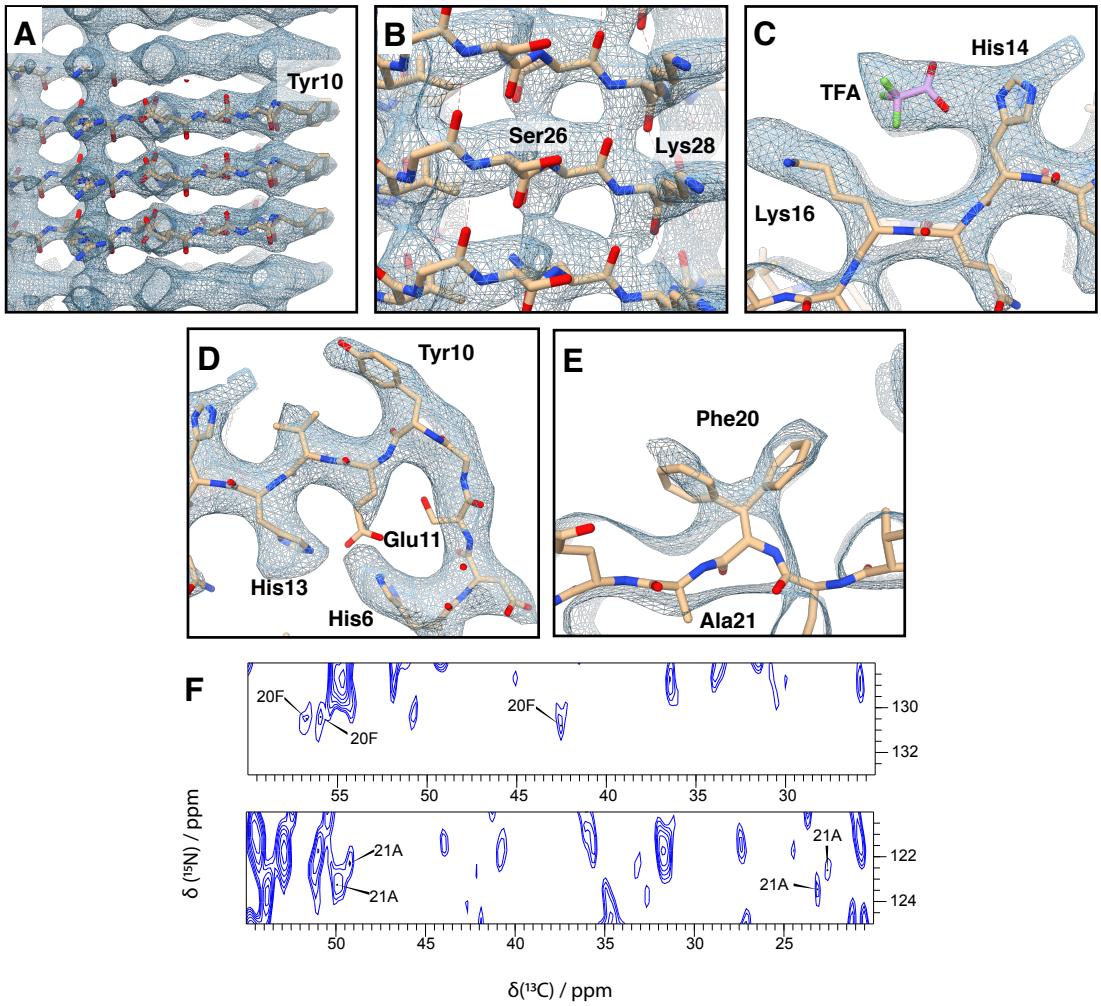

Fig. S8

Details of atomic model and density. (**A**) The density clearly resolves the separation of the individual β-strands along the fibril axis (density threshold 1σ). (**B**) The density of the ß-strands between to Ser26 and Lys28 is not clearly separated and might indicate the presence of a (less populated) second conformer (density threshold 1σ) (**C**) The extra density between the two positively charged sidechains of His14 and Lys16 most likely is a negatively charged trifluoroacetic acid molecule (density threshold 1.5σ). (**D**) The kink in the backbone at the Tyr10 is stabilized by salt-bridges between Glu11 with His6 and His13 as supported by NMR (table S3). Rat and mouse have three residue substitutions compared to human Aβ: R5G, Y10F, H13R. Whereas residues 5 and 10 are solvent exposed, any replacement of His13 might hinder the formation of the kink around Tyr10 (density threshold 1.5σ). (**E**) The presence of two rotamers of Phe20 is visible in the density map (density threshold 1.5σ), and (**F**) is also supported by the observed resonance doubling for Phe20 and for the neighboring residue Ala21 in the 2D NCACX correlation NMR spectrum.

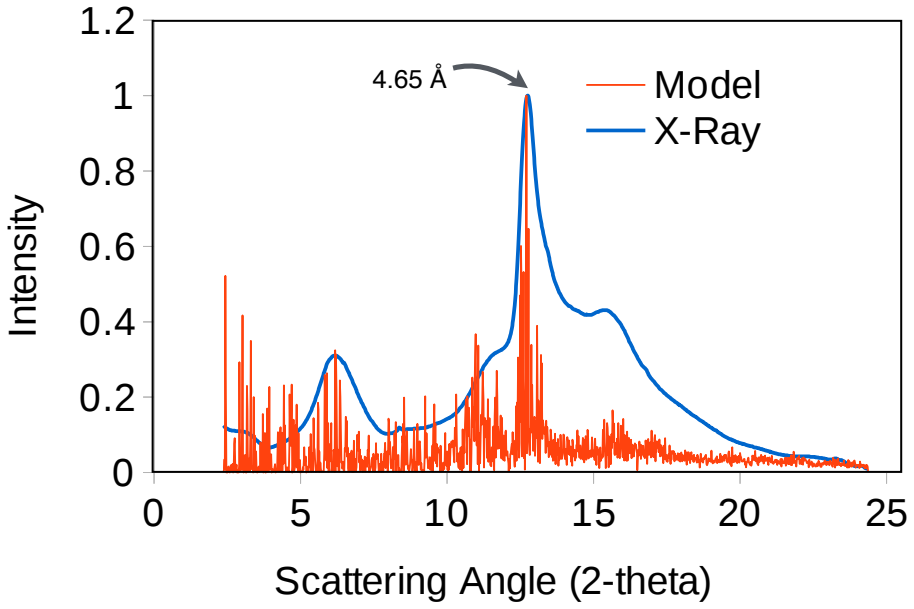

Fig. S9

Comparison of the atomic model with X-ray diffraction data. Radially averaged intensity profile from an X-ray diffraction experiment of the Aβ(1–42) fibrils. The measured profile (black) fits well to the intensity profile calculated from the atomic model (red). Based on the helical rise of 2.335 Å, the shift along the fibril axis between neighboring subunit layers within one protofilament is 4.67 Å, which is in excellent agreement with the strongest peak in the X-ray diffraction profile of 4.65 Å (see also Fig. 3C). The radial diffraction profile simulated from the atomic model agrees well with the experimental diffraction profile, suggesting that our model is a good representation of the complete fibril ensemble.

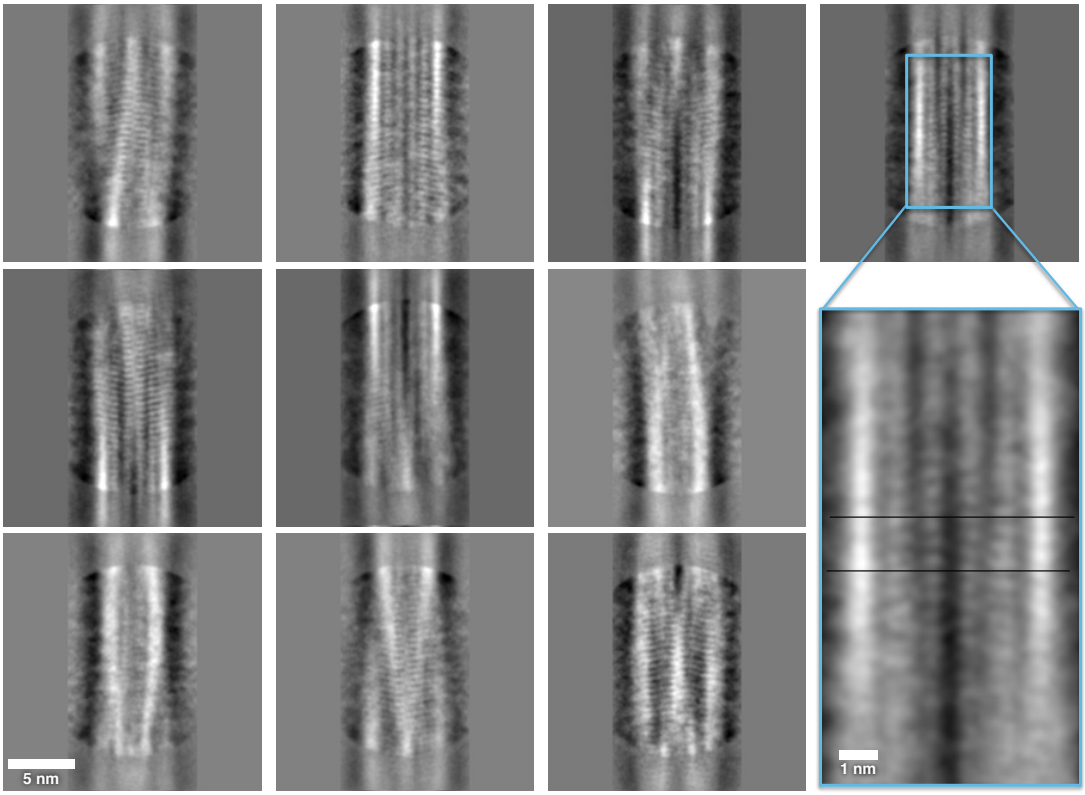

Fig. S10

2D Class averages of the fibrils. All 27,132 segments that were used for the final 3D reconstruction were used here for reference-free 2D class averaging with SPARX. The staggering of the subunits can clearly be seen (cf. close-up view, bottom right).

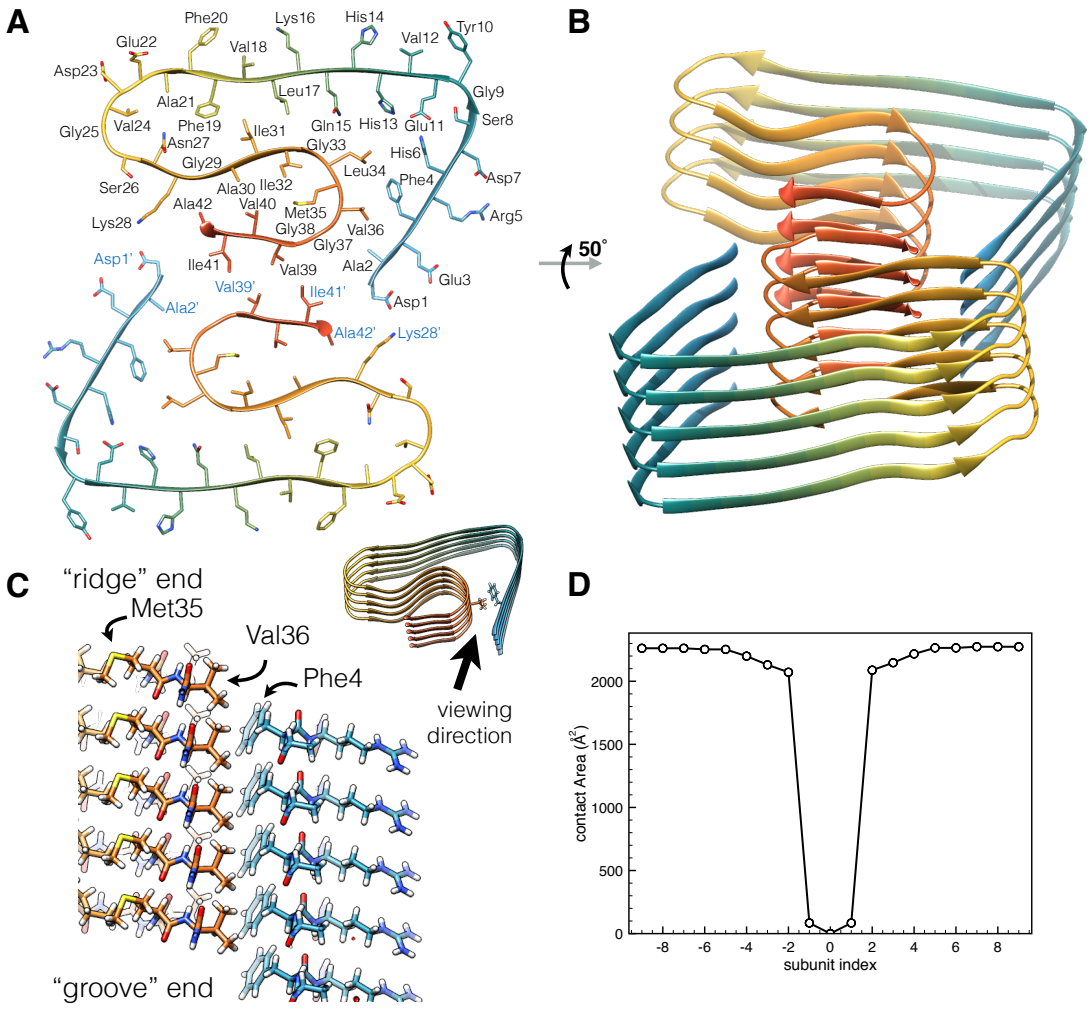

Fig. S11

Views of the atomic model and contact area analysis. (**A**) Cross-section of the Aβ(1–42) fibril showing two opposing subunits, one from each protofilament. (**B**) A view of the fragment of the fibril (comprising 9 subunits) that was used for the structure refinement (colored according to residue index). The buried surface area upon monomer addition of 2080 ± 50 Å^2 is the same for both fibril ends. (**C**) Side view into one protofilament, showing the staggered arrangement of the hydrophobic residues Phe4 and Val36 within the core of the protofilament. The methyl-group of Met35 possibly forms a hydrophobic contact with the methyl-groups of Met35 in the subunits above and below along the protofilament. Similarly, the residue Gln15 and Asn27 in subunit *i* forms hydrogen bonds with the corresponding residues in the neighboring subunits *i*-2 and *i*+2 (the subunit labeling used here is illustrated in Fig. 4A), resulting in glutamine and asparagine ladders that further stabilize the fibril (*1, 47*). (**D**) The minimal fibril unit. We define the minimal fibril unit as the minimal number of subunits that provide any additional subunit the same contact interface as an extended fibril does. The plot shows the surface area of subunit *i*

(subunit index = 0) buried upon successive addition of the respective subunit at the groove end (towards the left, negative subunit indices) or at the ridge end (towards the right, positive subunit indices). The plot illustrates that in both potential growth directions five subunits already provide the full interface for the next (sixth) monomer addition, i.e., the minimal fibril unit has a size of six subunits. We note that this definition of a minimal fibril unit is based on the observed fibril structure, and that the size of the minimal fibril unit may be an isomorph-specific quantity.

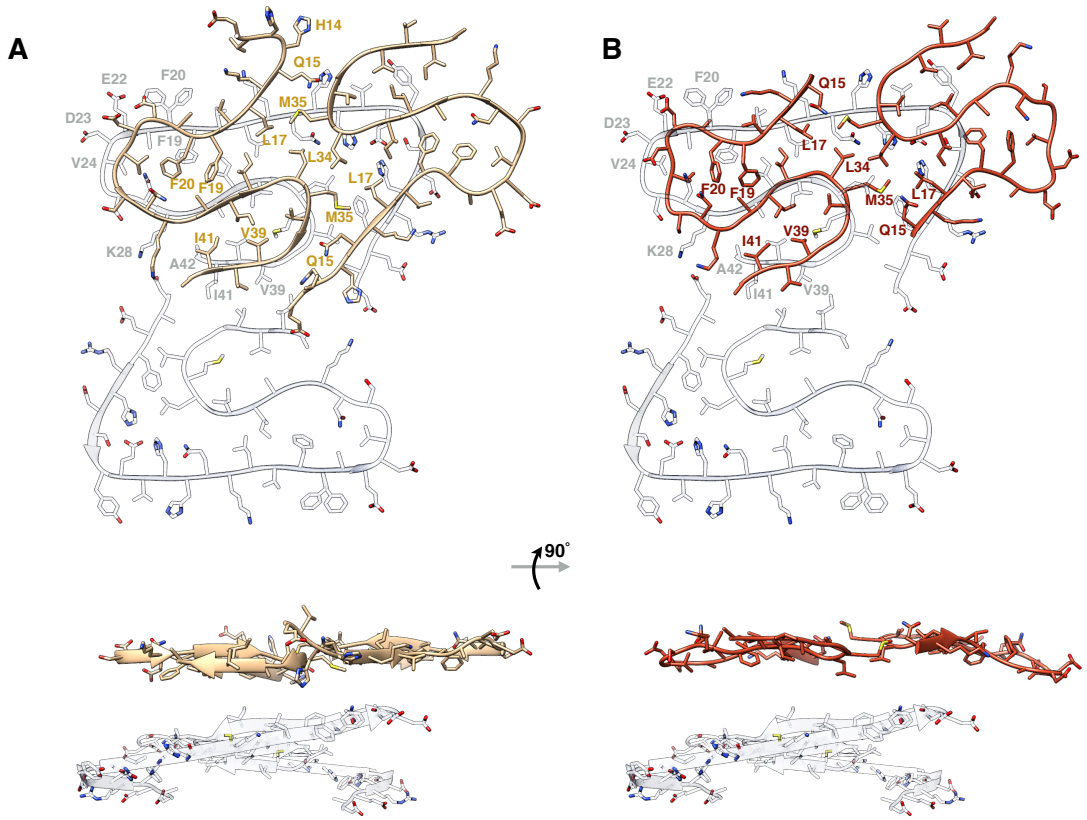

Fig. S12

Comparison with previous NMR structures. The C-terminal S-shape in the Aβ(1–42) fibril structure presented here (white) is similar to the NMR structures by (**A**) Colvin et al. (brown, PDB ID: 5KK3) (*11*) and (**B**) Wälti et al. (red, PDB ID: 2NAO) (*13*), however several sidechains point into different directions. The N-terminal region is not defined in the NMR structures. Side views are shown at the bottom, showing how the arrangement along the fibril axis is defined in the cryo-EM structure (white) as compared to the NMR structures (brown and red). NMR experiments cannot resolve the precise three-dimensional arrangement along the fibril axis, since they cannot assign intermolecular contacts to specific layers, the resulting models are therefore rather flat. The Cα-RMSD values (for residues 15-42 of a single subunit) between the model presented here and the structures by Colvin and Wälti are 2.9 Å and 3.2 Å, respectively, while the structures by Colvin and Wälti are much more similar to each other (RMSD value of 1.8 Å). Significant structural differences are also observed in the turn region of residues 20 to 25, which is also manifest in significant chemical shift differences observed in particular for residues Asp23 and Val24 (see also tables S4 and S5). While both Glu22 and Asp23 are exposed to the solvent also in the current structure, only Phe19 but not Phe20 is facing the hydrophobic core (see also Fig. 2). The dimer interface is completely different in the NMR structures, where the interface is mainly formed by Gln15, Leu17, Leu34, and Met35, and the sidechains of Val39 and Ile41 make

intramolecular rather than intermolecular contacts. The interfaces between one subunit with all neighboring (interacting) subunits in the different fibril models were analyzed with PDBePISA. The estimated solvation free energy gain upon formation of the interface ΔG is -30.4 kcal/mol and -28.8 kcal/mol for the NMR structures 2NAO and 5KK3, respectively (we removed the disordered amino acid residues 1-14 from the 2NAO model). For the Aβ(1–42) fibril structure presented here, the ΔG is -36.3 kcal/mol. ΔG does not include contributions from hydrogen bonds or salt bridges and is therefore a measure for the hydrophobicity of the interface.

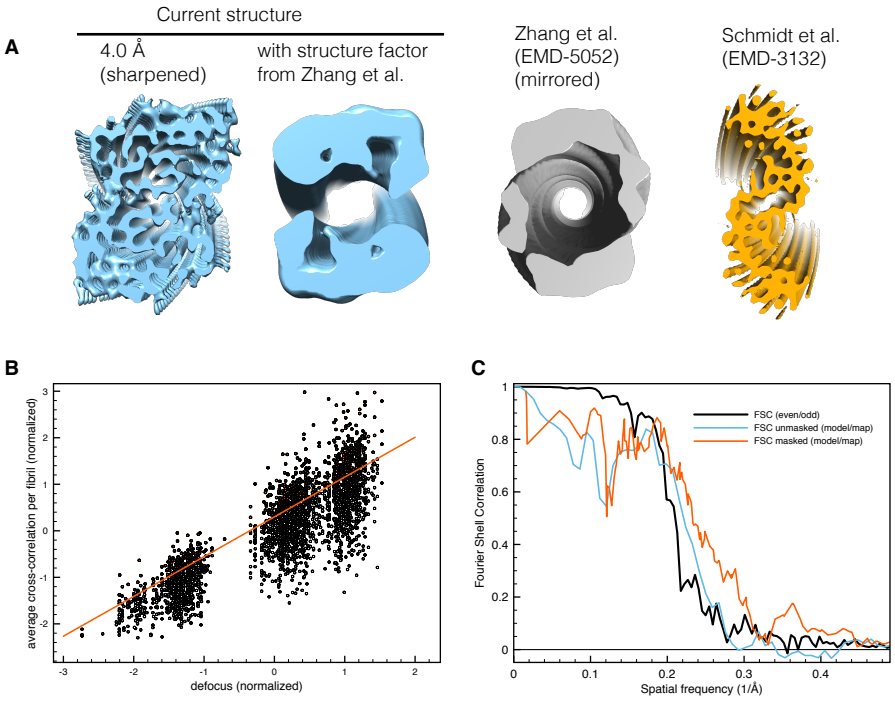

Fig. S13

EM image processing details. (**A**) Showing the cross-section of the current sharpened density map filtered to 4 Å (left, blue) and the current map to which the structure factor of the Zhang et al. (*21*) (EMD-5052) structure was applied (second from left, blue) for better comparison with the map by Zhang et al. (gray). If filtered to a similar low resolution, our model also appears to have a hollow core. The structure by Schmidt et al. (*9*) (EMD-3132, orange) seems to describe a different polymorph. (**B**) The selection of the best fibrils for the final reconstruction was done by calculating the average cross-correlation coefficient (CC) from projection matching. The CC values were plotted against defocus and those fibrils were chosen with an average CC value above the red line. The defocus and average cross-correlation values were normalized to have zero mean and a standard deviation of one. (**C**) The Fourier shell correlation (FSC) from the even/odd test (black) yields a resolution estimate of 4.0 Å using the 0.143-criterion. The 0.143-criterion is used here because two noisy half-maps are compared. The value is obtained from a fit of the function $1/[1+\exp((s-\beta) / \alpha)]$ with spatial frequency s. The comparison of the final atomic model with the full density map yields a very similar FSC curve (blue). The corresponding cross-resolution, r, (FSC(r)=0.5) of 4.5 Å for the full unmasked map and 4.1 Å for a map masked around nine Aβ subunits (red) is consistent with the FSC from the even/odd test. The 0.5-criterion needs to be used because a noisy full-map is compared with a noise-less (model) map.

Table S1.
Cryo-EM data collection and refinement statistics.

Data Collection	
Microscope	Tecnai Arctica
Voltage	200 kV
Camera	Falcon 3
Magnification	110,000
Defocus range (μm)	0.5 – 1.5
Electron dose (e/Å^2)	24
Exposure time (s)	2
Pixel size (Å)	0.935
Particle Statistics	
Filaments (total)	3179
Filaments (for final reconstruction)	813
Box size (px)	216
Segments	27,132
Aymmetric units	~295,000
Rise (Å)	2.335
Azimuthal rotation (º)	-179.275
Symmetry	C1
Model Composition	
Non-hydrogen atoms	2862
Number of chains	9
Refinement	
Resolution (Å)	4.0
Map CC (around atoms)	0.683
RMSD (bonds) (Å)	0.014
RMSD (angles) (º)	1.76
All-atom clashscore	7.41
Ramachandran outliers / favored (%)	0.0 / 80.0
Rotamer outliers	0 %
EMRinger score	5.1
Molprobity score	2.67

Table S2.

Experimental details of NMR experiments.

Sample: [*U*-^{13}C,^{15}N]- and recombinantly expressed Aβ(1-42)										
	HN CP	PDSD	SPC5_2	NCACX DARR	NCACB DREAM	NCOCX DARR	NCOCX DARR	NcoCAB BSH CP DREAM	NcoCAB BSH CP DREAM	PAR proton assisted recoupling
	1D	2D	2D	2D	2D	2D	3D	2D	3D	
Mixing time		1) 20 ms 2) 50 ms 3) 200 ms 4) 750 ms		55 ms		1) 100 ms 2) 107.5 ms	80 ms			15 ms
^{1}H frequency (MHz)	800	1) & 3) 800 2) & 4) 600	600	800	800	1) 600 2) 800	800	800	800	600
MAS (kHz)	18.00	1) & 3) 12.50 2) 11.00 4) 15.00	8.00	18.00	21.50	1) 14.00 2) 18.00	18.00	21.50	21.50	20.00
VT gas temperature (°C)	-10	-10	-10	-10	-10	-10	-10	-10	-10	0
Transfer 1	HN CP	HC CP	HC CP	HN CP	HN CP	HN CP	HN CP	HN CP	HN CP	HC CP
Carrier (ppm)	114.62	1) & 3) 73.14 2) 90.05 4) 109.00	70.53	119.99	119.91	1) 119.97 2) 119.91	119.91	119.91	119.91	70.52
Duration of 1st transfer (µs)	500	1) & 3) 500 2) 300 4) 400	300	500	660	1) 400 2) 780	660	760	660	300
Transfer 2			SPC5	N-CA CP	N-CA CP	N-CO CP	N-CO CP	N-CO CP	N-CO CP	PAR
Carrier (ppm)			Ca: 53.860 CO: 117.19	54.16	55.70	1) 174.42 2) 175.03	175.03	175.03	175.70	70.52
duration of 2nd transfer (µs)				2000	2600	1) 1400 2) 1325	1100	2600	2600	15000
^{13}C rf field (kHz)				4.71	7.45	1) 4.46 2) 3.42	7.24	7.66	7.55	46
^{15}N rf field (kHz)				11.41	11.76	1) 9.68 2) 12.93	9.27	11.96	12.21	
Transfer 3					DREAM			BSH CP	BSH CP	
Carrier (ppm)					55.70			56.03	60.60	
duration of 3rd transfer (µs)					1875			3800	3750	

^{13}C rf field (kHz)								13.97	14.69	
Transfer 4								DREAM	DREAM	
Carrier (ppm)								56.43	57.5	
duration of 4th transfer (µs)								1800	1850	
t_1 increments	182	1) & 3) 1250 2) 454 4) 357	908	1250	714	1) 1072 2) 1406	882	882	714	233
t_1 spectral width (kHz)	18.116	1) & 3) 104.167 2) 37.879 4) 44.643	37.878	104.167	59.524	1) 89.286 2) 78.125	73.529	73.529	59.524	44.643
t_2 increments		1) & 3) 240 2) 198 4) 270	240	22	20	1) 20 2) 22	12	20	12	225
t_2 spectral width (kHz)		1) & 3) 40.225 2) 33.281 4) 45.000	40.080	2.999	3.200	1) 3.600 2) 3.000	2.400	3.200	2.400	45
t_3 increments							20		15	
t_3 spectral width (kHz)							5.000		5.000	
Number of scans		1) 80, 3) 160 2) 192 4) 176	Ca: 224 CO: 256	6656	800	1) 4672 2) 7840	544	5376	1376	624
Duration	1.75 h	1) 21.75 h 2) 43.7 h 3) 47.25 h 4) 73.00 h	Ca: 43.5 h CO: 69.5 h	168.6 h	18 h	1) 43.6 h 2) 110 h	304.5 h	121 h	557.5 h	157.75 h

Table S3.

Chemical shifts for Aβ(1–42) fibrils.

		N	C‘	Cα	Cβ	Cγ	Cδ	Cε	Cξ	Nδ1	Nδ2	Nε1	Nε2	Nξ	NH1	NH2
1	D		172.0	55.0	41.9	180.1										
2	A	121.9	175.6	51.0	24.5											
3	E	116.1	173.6	54.4	32.0	33.7										
4	F	121.5	172.5	56.6	42.3	137.9	131.6									
5	R	121.2	173.6	54.6	33.9	27.5	43.9		159.3			84.6			72.7	70.5
6	H	127.3	173.8	51.4	33.3	132.5				182.8			176.3			
7	D	121.5	173.2	52.0	41.2	179.3										
8	S	117.0	175.0	55.3	66.3											
9	G	111.8	174.0	47.3												
10	Y	124.8	173.8	56.8	41.6		133.0	118.4	157.0							
11	E	125.5	173.7	54.6	33.4	35.0	182.6									
12	V	124.5	174.1	60.4	34.8	21.1, 20.1										
13	H	126.7	172.8	51.4	31.9	131.8	117.3	137.7		182.8			176.3			
14	H	127.3	174.1	51.2	32.7	132.7	115.1			182.8			176.3			
15	Q	121.6	173.9	53.1	31.9	33.1	179.2									
16	K	123.8	173.3	54.5	39.0	26.0	31.5	42.4						33.8		
17	L	128.6	175.1	54.9	45.0	31.4	27.2, 24.4									
18	V	121.5	176.4	60.6	35.4	21.0, 22.2										
19	F	122.2	172.6	56.6	44.2	137.6	131.5, 132.9									
20	F	130.2	172.5	56.3	42.5	138.1	131.3									
20'	F	130.2	172.5	56.0	42.5	138.1	131.3									
21	A	122.5	174.9	49.2	22.3											
21'	A	123.5	176.3	49.6	23.1											
22	E	121.3	173.5	54.5	33.5	38.1	182.7									
23	D	126.7	174.1	53.9	35.1	177.0										
24	V	118.8	175.8	58.1	36.7	21.1, 23.1										
25	G	116.3	174.6	49.0												
26	S		172.4	56.6	65.9											
26'	S	115.1	172.7	56.1	65.4											
27	N	119.7	175.6	52.4	41.4	178.1					109.6					
28	K	128.6	175.5	54.9	36.4	26.1	30.1	42.1						33.8		
29	G	111.6	170.5	44.7												
30	A	120.6	173.8	49.8	23.6											
31	I	121.5	174.6	60.1	40.8	27.3, 17.5	14.7									
32	I	125.0	176.0	57.5	42.7	27.0, 18.1	15.2									
33	G	113.7		44.8												
34	L	126.0	173.5	54.5	45.4	27.9	25.4, 24.3									
35	M	126.5	173.5	54.3	37.9	32.1		17.3								
36	V	126.3	175.5	60.2	35.2	20.6, 21.2										
37	G	114.6	173.1	49.0												
38	G	116.0	173.2	48.9												
39	V	125.4	173.4	60.4	33.9	21.4, 20.8										
40	V	126.8	174.0	60.4	35.2	21.7, 20.5										
41	I	126.3	175.7	59.1	41.8	27.4, 17.2	13.4									
42	A	126.8	179.4	49.3	21.2											

Table S4.

Chemical shift differences between Wälti et al.(*13*) and this work (ppm).

		N	C‘	Cα	Cβ	Cγ(1)	Cγ(2)	Cδ(1)	Cδ(2)	Cε(1)
1	D	-	-0.03	-0.85	-0.36	-1.17	-	-	-	-
2	A	-4.89	-0.55	-0.42	-0.65	-	-	-	-	-
3	E	1.22	-0.11	0.21	1.39	2.16	-	-	-	-
4	F	-1.18	2.83	0.29	-0.65	1.63	-	-	-	-
5	R	1.62	0.98	0.66	-0.76	-0.09	-	-	-	-
6	H	-0.30	0.77	-0.43	-2.89	1.86	-	-	-	-
7	D	4.26	4.03	6.87	-2.11	0.65	-	-	-	-
8	S	-7.97	-1.62	1.35	-1.86	-	-	-	-	-
9	G	0.54	-0.55	-4.02	-	-	-	-	-	-
10	Y	-3.96	0.85	0.34	-5.88	-	-	0.21	-	-0.97
11	E	-	-	-	-	-	-	-	-	-
12	V	-	-	-	-	-	-	-	-	-
13	H	-	-	-	-	-	-	-	-	-
14	H	-	-	-	-	-	-	-	-	-
15	Q	3.43	-0.05	1.04	-0.42	1.04	-	-1.52	-	-
16	K	0.12	-1.06	0.29	-1.35	-	-	-	-	-
17	L	1.21	-0.19	-0.20	0.18	-2.25	-	-1.25	-1.55	-
18	V	2.17	-2.22	-1.01	0.30	-0.14	-1.34	-	-	-
19	F	6.34	2.14	3.57	-3.56	2.20	-	-0.49	-	-
20	F	-14.79	2.10	0.48	-2.16	1.81	-	2.75	-	-
21	A	-0.92	2.27	3.54	-1.69	-	-	-	-	-
22	E	-4.99	1.91	-0.11	-1.09	-2.65	-	-1.92	-	-
23	D	-6.67	1.58	1.96	6.23	3.21	-	-	-	-
24	V	-2.52	1.37	1.19	-0.91	1.93	-2.25	-	-	-
25	G	-0.66	-0.48	-0.84	-	-	-	-	-	-
26	S	-3.24	0.15	0.18	0.34	-	-	-	-	-
27	N	-2.74	-1.56	0.74	1.59	-2.68	-	-	-	-
28	K	0.60	-0.04	0.09	-1.07	0.58	-	0.52	-	0.22
29	G	-0.55	0.90	3.88	-	-	-	-	-	-
30	A	2.99	2.28	1.02	-1.93	-	-	-	-	-
31	I	-2.11	-0.86	-0.38	3.86	0.41	1.36	-0.01	-	-
32	I	-0.94	-1.51	2.61	-1.33	0.69	0.95	-0.66	-	-
33	G	-4.64	-	0.98	-	-	-	-	-	-
34	L	-16.84	5.25	2.62	-3.37	-1.53	-	-3.98	3.31	-
35	M	-10.34	-0.14	0.67	-1.10	-1.17	-	-	-	-0.03
36	V	-3.71	-0.35	0.52	-0.67	0.57	-0.70	-	-	-
37	G	-0.68	-0.46	-3.62	-	-	-	-	-	-
38	G	-3.42	1.95	-0.18	-	-	-	-	-	-
39	V	-8.90	0.68	-0.87	1.34	-0.50	0.10	-	-	-
40	V	-1.64	0.03	0.74	0.58	-0.54	0.66	-	-	-
41	I	0.27	-2.08	0.93	-1.71	0.60	2.08	1.23	-	-
42	A	4.03	2.64	3.91	2.37	-	-	-	-	-

Table S5.

Chemical shift differences between Colvin et al.(*11*) and this work (ppm).

		N	C‘	Cα	Cβ	Cγ(1)	Cγ(2)	Cδ(1)	Cδ(2)	Cε(1)
1	D	-	-	-0.72	0.36	-	-	-	-	-
2	A	-	-	1.43	-5.51	-	-	-	-	-
3	E	-	-	2.09	-2.17	2.24	-	-	-	-
4	F	-	-	-1.58	-3.19	-	-	-	-	-
5	R	0.70	2.90	-0.51	-0.76	-0.40	-	-	-	-
6	H	-	-	-	-	-	-	-	-	-
7	D	-	-1.04	-	-	-	-	-	-	-
8	S	-3.80	-2.06	-0.23	-0.16	-	-	-	-	-
9	G	-1.14	-1.80	0.94	-	-	-	-	-	-
10	Y	-11.80	3.00	-1.80	-0.25	-	-	-0.60	-	-1.20
11	E	-5.00	-	-2.06	2.26	-2.57	-	-	-	-
12	V	0.10	-2.00	-0.15	-	-	-	-	-	-
13	H	-	-	-	-	-	-	-	-	-
14	H	-	-	-	-	-	-	-	-	-
15	Q	-	-	-	-	-	-	-	-	-
16	K	0.73	-1.52	0.03	-	-0.29	-	-1.32	-	-
17	L	3.49	-0.69	-0.70	-0.24	-2.69	-	-4.76	1.05	-
18	V	3.73	-2.69	-1.66	-0.21	-0.70	-	-	-	-
19	F	8.15	1.78	3.29	-3.91	2.01	-	-1.00	-	-
20	F	-13.02	1.74	0.03	-2.25	1.27	-	-0.70	-	-
21	A	0.97	1.79	3.05	-2.02	-	-	-	-	-
22	E	-2.76	1.84	-0.47	-0.44	-2.25	-	0.90	-	-
23	D	-4.75	1.26	1.52	5.88	2.95	-	-	-	-
24	V	-0.85	0.98	0.76	-1.38	-0.70	-0.54	-	-	-
25	G	0.91	-0.87	-1.29	-	-	-	-	-	-
26	S	-1.81	-0.29	-0.17	-0.06	-	-	-	-	-
27	N	-1.17	-1.84	0.41	1.30	-	-	-	-	-
28	K	1.65	-0.33	-0.14	-1.36	-0.10	-	-0.29	-	-0.06
29	G	0.88	0.56	3.46	-	-	-	-	-	-
30	A	4.49	1.92	0.45	-2.34	-	-	-	-	-
31	I	-0.44	-1.22	-0.80	3.22	0.05	1.15	-0.63	-	-
32	I	0.74	-1.88	2.17	-1.75	0.32	0.54	-1.09	-	-
33	G	-2.94	-	0.59	-	-	-	-	-	-
34	L	-15.32	4.76	2.20	-3.70	-0.76	0.00	-4.48	1.69	-
35	M	-7.86	-0.51	0.18	-1.52	-1.48	0.00	-	-	-0.30
36	V	-1.70	-0.82	-0.05	-0.68	-1.71	0.62	-	-	-
37	G	0.77	0.20	-3.96	-	-	-	-	-	-
38	G	-5.25	1.10	-0.68	-	-	-	-	-	-
39	V	3.75	1.10	0.73	0.77	-1.18	0.33	-	-	-
40	V	1.38	-0.23	0.43	-0.64	-1.00	-0.18	-	-	-
41	I	1.15	-2.67	0.48	-2.32	-	1.41	0.78	-	-
42	A	7.34	2.68	3.21	-0.92	-	-	-	-	-

Table S6.

Chemical shift differences between Xiao et al.(*14*) and this work (ppm).

		N	C‘	Cα	Cβ	Cγ(1)	Cγ(2)	Cδ(1)	Cδ(2)	Cε(1)
1	D	-	-	-	-	-	-	-	-	-
2	A	-	-2.00	-0.50	-6.9	-	-	-	-	-
3	E	-	-	-	-	-	-	-	-	-
4	F	2.10	0.50	-1.60	-2.30	-0.10	-	-	-	-
5	R	-	-	-	-	-	-	-	-	-
6	H	-	-	-	-	-	-	-	-	-
7	D	-	-	-	-	-	-	-	-	-
8	S	-	-	-	-	-	-	-	-	-
9	G	-2.60	-3.50	-4.00	-	-	-	-	-	-
10	Y	-	-	-	-	-	-	-	-	-
11	E	-	-	-	-	-	-	-	-	-
12	V	0.80	-1.80	-1.40	-1.20	-1.80	-0.80	-	-	-
13	H	-3.20	-0.90	1.00	-1.90	4.00	-	-2.30	-	-
14	H	-2.90	-1.90	0.90	-2.20	5.00	-	2.10	-	-
15	Q	-	-	-	-	-	-	-	-	-
16	K	-	-	-	-	-	-	-	-	-
17	L	3.70	-2.20	-2.00	-1.80	-4.20	-	-3.20	-3.60	-
18	V	3.70	-4.50	-3.00	-1.90	-2.30	-3.50	-	-	-
19	F	8.00	0.30	2.20	-5.10	0.10	-	-3.00	-	-
20	F	-12.30	0.10	-1.10	-4.00	-0.30	-	0.80	-	-
21	A	1.70	0.40	2.00	-3.50	-	-	-	-	-
22	E	-	-	-	-	-	-	-	-	-
23	D	-4.50	-0.50	-0.10	4.50	1.10	-	-	-	-
24	V	-0.20	-0.80	-0.50	-2.60	0.20	-4.00	-	-	-
25	G	1.20	-2.40	-2.50	-	-	-	-	-	-
26	S	-0.10	-2.40	-1.70	-1.60	-	-	-	-	-
27	N	-	-	-	-	-	-	-	-	-
28	K	2.70	-2.30	-2.30	-3.10	-1.90	-	-1.80	-	-2.00
29	G	2.00	-1.10	1.90	-	-	-	-	-	-
30	A	5.40	0.10	-0.80	-3.60	-	-	-	-	-
31	I	0.20	-2.70	-1.90	1.80	-1.50	-0.60	-2.20	-	-
32	I	1.50	-3.70	0.80	-3.20	-1.20	-1.40	-2.80	-	-
33	G	-2.40	-	-0.40	-	-	-	-	-	-
34	L	-14.50	3.10	0.90	-5.30	-3.00	-	-2.80	-4.60	-
35	M	-	-	-	-	-	-	-	-	-2.00
36	V	-1.90	-2.30	-1.30	-2.40	-1.50	-2.70	-	-	-
37	G	1.60	-2.60	-5.40	-	-	-	-	-	-
38	G	-2.40	-1.70	-2.10	-	-	-	-	-	-
39	V	-5.10	-1.50	-2.10	0.10	-2.50	-1.90	-	-	-
40	V	0.80	-2.20	-1.30	-1.90	-2.70	-1.50	-	-	-
41	I	2.30	-4.50	-0.80	-4.00	-1.60	-0.10	-0.80	-	-
42	A	-	0.60	1.50	-1.90	-	-	-	-	-

Table S7.

Chemical shift differences (ppm) between this work and Qiang et al. (45) after adjustment of ^{13}C chemical shifts. Differences were computed between this work and Table in Extended Data Figure 8 of Qiang et al. (45), columns [Aβ42 "a"] and [Aβ42 "b"].

Comparison with [Aβ42 "a"]							
		N	Cα	Cβ	Cγ(1)	Cγ(2)	Cδ(1)
19	F	-2.8	< 0.1	0.6			
25	G	-0.6	-2.7				
30	A	0.1	2.9	2.6			
31	I	-1.7	2.4	3.8	3.1	2.7	2.7
34	L	0.2	1.0	1.2	1.9		
35	M	< 0.1	1.9	-1.2	2.1		
Comparison with [Aβ42 "b"]							
		N	Cα	Cβ	Cγ(1)	Cγ(2)	Cδ(1)
19	F	7.8	2.3	-0.5			
25	G	-1.5	-1.3				
30	A	6.5	2.3	0.4			
31	I	3.1	2.2	1.7	2.7	2.1	1.2
34	L	-2.5	1.5	2.5	2.5		
35	M	0.4	2.0	1.3	2.4		

Movie S1:
Showing the density map of the fibril (corresponding to Fig. 1A).

Movie S2:
Showing the ridge end of the fibril (corresponding to Fig. 4C).

Movie S3:
Showing the groove end of the fibril (corresponding to Fig. 4D).